

# The Helmholtz Dirichlet and Neumann problems on piecewise smooth open curves

Johan Helsing<sup>a</sup>, Shidong Jiang<sup>b</sup>

<sup>a</sup>*Centre for Mathematical Sciences, Lund University  
Box 118, 221 00 Lund, Sweden*

<sup>b</sup>*Center for Computational Mathematics, Flatiron Institute, Simons Foundation  
New York, NY 10010, USA*

---

## Abstract

A numerical scheme is presented for solving the Helmholtz equation with Dirichlet or Neumann boundary conditions on piecewise smooth open curves, where the curves may have corners and multiple junctions. Existing integral equation methods for smooth open curves rely on analyzing the exact singularities of the density at endpoints for associated integral operators, explicitly extracting these singularities from the densities in the formulation, and using global quadrature to discretize the boundary integral equation. Extending these methods to handle curves with corners and multiple junctions is challenging because the singularity analysis becomes much more complex, and constructing high-order quadrature for discretizing layer potentials with singular and hypersingular kernels and singular densities is nontrivial. The proposed scheme is built upon the following two observations. First, the single-layer potential operator and the normal derivative of the double-layer potential operator serve as effective preconditioners for each other locally. Second, the recursively compressed inverse preconditioning (RCIP) method can be extended to address "implicit" second-kind integral equations. The scheme is high-order, adaptive, and capable of handling corners and multiple junctions without prior knowledge of the density singularity. It is also compatible with fast algorithms, such as the fast multipole method. The performance of the scheme is illustrated with several numerical examples.

*Keywords:* Helmholtz equation, Dirichlet problem, Neumann problem, open surface problem, integral equation method, RCIP method

*2000 MSC:* 31A10, 45B05, 45E99, 65N99, 65R20

---

---

*Email addresses:* [johan.helsing@math.lth.se](mailto:johan.helsing@math.lth.se) (Johan Helsing),  
[sjiang@flatironinstitute.org](mailto:sjiang@flatironinstitute.org) (Shidong Jiang)

## 1. Introduction

In this paper, we consider the time-harmonic wave scattering problem from a collection of open curves in two dimensions. The governing partial differential equation (PDE) for the scattered field  $u$  is the Helmholtz equation:

$$\Delta u(r) + k^2 u(r) = 0, \quad r = (x, y) \in \mathbb{R}^2 \setminus \Gamma, \quad (1)$$

with the Sommerfeld radiation condition

$$\lim_{|r| \rightarrow \infty} \sqrt{|r|} \left( \frac{\partial}{\partial |r|} - ik \right) u(r) = 0 \quad (2)$$

imposed at infinity. Here,  $k$  is the wavenumber, and the boundary  $\Gamma$  consists of a set of piecewise smooth open curves. By “piecewise smooth”, we mean that these curves may have corners and branch points, such as triple junctions, quadruple junctions, et cetera. On the boundary, we impose either the Dirichlet condition

$$u(r) = g(r), \quad r \in \Gamma, \quad (3)$$

or the Neumann condition

$$\frac{\partial u}{\partial \nu}(r) = g(r), \quad r \in \Gamma, \quad (4)$$

where  $\nu$  is the unit normal vector at  $r$ . These problems are frequently encountered in acoustic and electromagnetic scattering. In acoustics, the Dirichlet condition corresponds to a sound-soft object, and the Neumann condition corresponds to a sound-hard object. In electromagnetics, they correspond to planar transverse electric (TE) and transverse magnetic (TM) waves, respectively [6, 20].

Boundary integral methods are standard tools for solving the Helmholtz Dirichlet and Neumann problems due to several advantages. First, the radiation condition is satisfied automatically by the layer potential representation of the field, removing the need of truncating the computational domain and constructing the so-called artificial boundary conditions. Second, the densities of layer potentials are supported on the boundary, leading to an optimal number of unknowns during the solve phase. Third, the far-field pattern can be evaluated accurately and efficiently via the integral representation and fast algorithms, such as the fast multipole method (FMM) [9, 10, 16, 42, 43]. Among all possible integral formulations, second-kind integral equations (SKIEs) have become popular in the last two or three decades due to their well-conditioning, which leads to stable and improved accuracy and a low number of iterations for iterative solvers such as GMRES [44].

There are two main difficulties associated with piecewise smooth open curves. First, there is a fundamental change in topology between closed curves and open curves. A closed curve divides the entire space into two domains – the interior and the exterior. When the curve is open, there is no distinction between the interior and the exterior. Thus, the so-called lightning solver [14], a special

case of method of fundamental solutions [4], cannot be applied to solve these problems. This is because the poles in those methods must be placed outside the domain where the solution is sought, and the domain for the open-curve problem is the entire space. For closed curves, the construction of SKIEs relies on the so-called jump relations of layer potentials in potential theory. For open curves, however, the field must be continuous across the boundary for the Dirichlet problem. And its normal derivative must be continuous across the boundary for the Neumann problem. Thus, classical integral representations, which induce jumps across the boundary, cannot be used for open curves. Furthermore, the endpoints of an open curve introduce strong singularity in the density of layer potentials, often changing the underlying function space and complicating the design of numerical procedures.

Second, the singularity analysis of densities at corners and branch points is rather difficult. Indeed, for the boundary integral equation (BIE) formulation of the Helmholtz equation, the singularity analysis at corners has been done only recently [30, 46, 47, 48]. Since the analysis depends on the governing equation, the boundary condition, and the type of point singularity, it is carried out for each particular case. See, for example, [28] for the Laplace equation with Neumann boundary conditions, [41] for the Stokes equation with corners, and [29] for the Laplace equation with triple junctions. The subsequent quadrature design, following the singularity analysis, requires considerable effort. This is because the density often contains infinitely many types of singularities that depend on the opening angle, say, in the case of corners. Even with the use of generalized Gaussian quadrature [5, 36, 53], a special quadrature must be constructed for each specific case to ensure that the number of quadrature nodes is not excessively large. The construction of these special quadratures is usually not performed on the fly, as the precomputation of tables is costly in terms of computation and storage.

In this paper, we propose a numerical scheme for solving the Helmholtz Dirichlet and Neumann problems on open curves. The scheme is based on the following two observations. First, the single layer potential operator  $S_k$  (defined in (6)) and the normal derivative of the double layer potential operator  $T_k$  (defined in (8)) (or more generally, hypersingular operators including the quadruple layer potential operator [33]) are good preconditioners of each other. For closed curves, these are two well-known Calderón identities from the Calderón projector [8, 31]. In [12, 49], it is shown that the densities of the single-layer and hypersingular integral operators have inverse square root and square root singularity in the vicinity of the endpoints, respectively. In [6], the authors generalize these Calderón identities to the case of open curves by pulling out the aforementioned singularities explicitly from the densities. However, it is nontrivial to extend the work in [6] to treat the case of piecewise smooth open curves, where the corners and branch points lead to additional difficulties. In [17], a *local* analysis is carried out to generalize the Poincaré–Bertrand formula on a hypersurface. As the analysis is mostly local, a similar argument can be used to show that  $S_k$  and  $T_k$  are good preconditioners to each other locally. Second, the recursively compressed inverse preconditioning (RCIP) method, first

introduced in [23], has proven to be highly successful in handling all types of point singularities for BIEs in two dimensions. See [19] and references therein. The RCIP method provides a unified framework for addressing these challenging problems accurately and efficiently, without requiring any analysis of the exact singularities in the densities of layer potentials.

Our scheme combines these two observations in a straightforward manner. We apply  $T_k$  to precondition  $S_k$  for the Dirichlet problem, and  $S_k$  to precondition  $T_k$  for the Neumann problem. Unlike [6], we do not explicitly extract the singularities from the densities. Although the authors of [6] successfully extracted the singularities of the densities for smooth open curves, doing so would be rather cumbersome numerically in the presence of corners and branch points. Instead, we apply the RCIP method to uniformly treat the endpoint and other point singularities. We then divide the open curves into panels and apply a high-order kernel-split quadrature [22, 24] to discretize the layer potentials. It turns out that the RCIP method is capable of figuring out the correct function spaces in a remarkable way. Furthermore, even though the formulation is of the second-kind *implicitly*, we have not observed any GMRES stagnation [1] due to the lack of numerical second-kindness in our numerical experiments. The resulting numerical scheme is accurate, efficient, and fully adaptive. It can also be easily coupled with fast algorithms, such as the FMM, to solve large-scale problems. On the other hand, it seems rather difficult to extend the global spectral discretization scheme presented in [6] to handle corners and branch points, which may also have a compatibility issue with fast algorithms [18].

The rest of the paper is organized as follows. In Section 2, we summarize the notations, analytical and numerical tools, and the results in [6] for comparison purpose. In Section 3, we present our numerical scheme. Numerical examples are shown in Section 4.

## 2. Preliminaries

### 2.1. Green's function and layer potentials

The free-space Green's function, also called fundamental solution, of the Helmholtz equation in  $\mathbb{R}^2$  is

$$\Phi_k(r, r') = \frac{i}{4} H_0^{(1)}(k|r - r'|). \quad (5)$$

Here  $k$  is a wavenumber,  $r = (x, y)$ , and  $H_0^{(1)}$  is the zeroth order Hankel function of the first kind [40].

Let  $\Gamma$ , as above, be a set of piecewise smooth open curves, referred to collectively as the *boundary*. The unit normal at  $r \in \Gamma$  is  $\nu(r)$ . We use standard definitions of the Helmholtz layer potential operators  $S_k$ ,  $K_k$ , and  $T_k$  [11, pp. 41–

42], defined by their action on a layer density  $\rho(r)$  on  $\Gamma$  as

$$S_k \rho(r) = 2 \int_{\Gamma} \Phi_k(r, r') \rho(r') \, d\ell', \quad r \in \Gamma, \quad (6)$$

$$K_k \rho(r) = 2 \int_{\Gamma} \frac{\partial \Phi_k}{\partial \nu'}(r, r') \rho(r') \, d\ell', \quad r \in \Gamma, \quad (7)$$

$$T_k \rho(r) = 2 \int_{\Gamma} \frac{\partial^2 \Phi_k}{\partial \nu \partial \nu'}(r, r') \rho(r') \, d\ell', \quad r \in \Gamma, \quad (8)$$

where  $d\ell$  is an element of arc length,  $\partial/\partial\nu = \nu(r) \cdot \nabla$ , and  $\partial/\partial\nu' = \nu(r') \cdot \nabla'$ . For ease of presentation we also use  $S_k$  and  $K_k$  to define single- and double-layer potentials. That is, we use

$$S_k \rho(r) = 2 \int_{\Gamma} \Phi_k(r, r') \rho(r') \, d\ell', \quad r \in \mathbb{R}^2 \setminus \Gamma, \quad (9)$$

$$K_k \rho(r) = 2 \int_{\Gamma} \frac{\partial \Phi_k}{\partial \nu'}(r, r') \rho(r') \, d\ell', \quad r \in \mathbb{R}^2 \setminus \Gamma. \quad (10)$$

### 2.2. Calderón identities on closed curves

From [11, p. 43] we have on closed curves

$$S_k(-T_k) = I - K_k K_k, \quad r \in \Gamma, \quad (11)$$

$$T_k(-S_k) = I - K_k^A K_k^A, \quad r \in \Gamma, \quad (12)$$

where  $I$  is the identity operator, and  $K_k^A$  is defined by

$$K_k^A \rho(r) = 2 \int_{\Gamma} \frac{\partial \Phi_k}{\partial \nu}(r, r') \rho(r') \, d\ell', \quad r \in \Gamma. \quad (13)$$

### 2.3. Summary of the work in [6]

Here, we provide a short summary of the work by Bruno and Lintner in [6]. The main purpose is to make the comparison between our numerical scheme and the scheme in [6] easy and transparent. Suppose now that  $\Gamma$  is a smooth open curve with the parameterization  $r(t) = (x(t), y(t))$  for  $t \in [-1, 1]$ . Define the weight function  $\omega$  by

$$\omega(r(t)) = \sqrt{1 - t^2}. \quad (14)$$

Using the singularity analysis from [12, 49], Bruno and Lintner propose to pull out the singularity from the density explicitly from  $S_k$  and  $T_k$ . To be more precise, they consider the weighted operators

$$S_k^\omega[\rho](r) = S_k \left[ \frac{\rho}{\omega} \right](r), \quad T_k^\omega[\rho](r) = T_k[\omega\rho](r). \quad (15)$$

For the Dirichlet problem, the field is represented as

$$u(r) = S_k^\omega[\rho](r), \quad r \in \mathbb{R}^2 \setminus \Gamma, \quad (16)$$

and the BIE is

$$T_k^\omega S_k^\omega \rho = T_k^\omega g. \quad (17)$$

For the Neumann problem, the field is represented as

$$u(r) = K_k^\omega S_k^\omega [\rho](r), \quad r \in \mathbb{R}^2 \setminus \Gamma, \quad (18)$$

and the BIE is

$$T_k^\omega S_k^\omega \rho = g. \quad (19)$$

The BIEs (17,19) are further analyzed with the cosine transform  $t = \cos \theta$  and an even extension mapping the interval  $[-1, 1]$  to  $[0, 2\pi]$ , so that standard Calderón identity (12) can be used. On the numerical side, these BIEs are discretized via a global spectral method using the fact that the convolution of the logarithmic kernel with trigonometric basis functions can be evaluated analytically [34], which is equivalent to the fact that the convolution integral of  $\int_{-1}^1 \ln|x-t|T_n(t)/\sqrt{1-t^2}dt$  can be evaluated analytically (see, for example, [32, eqs. (27)-(28)]). The authors further observe that the system matrix can be constructed in  $O(N^2 \ln N)$  operations with the FFT, where  $N$  is the total number of discretization points on  $\Gamma$ .

The analysis in [6] and the subsequent paper [35] is fairly complete, although there are some drawbacks with the associated numerical scheme. First, it is not clear how one could reduce the computational cost from  $O(N^2 \ln N)$  to  $O(N \ln N)$ . A global kernel-split quadrature is applied to discretize the associated integral operators. According to [18], the quadrature scheme seems incompatible with the use of fast algorithms such as the FMM. Second, being a global discretization scheme, it is inefficient to handle fine local structure in the geometry and data. Third, there is no discussion on the evaluation of the near field, though it is well-known that close evaluation is actually most difficult in the design of high-order quadratures for the evaluation of singular and nearly singular integrals. Finally and most importantly, it is rather difficult to extend the analysis and numerical scheme in [6] to treat open curves with corners and branch points, as discussed in Section 1.

#### 2.4. Overview of RCIP

The RCIP method accelerates and stabilizes Nyström solvers in certain “singular” situations. More precisely, RCIP applies to the Nyström discretization of Fredholm second kind BIEs on closed or open  $\Gamma$  that contain some type of singular points. These points could be endpoints, corners, or branch points of  $\Gamma$ . This section, based on [19, Sections 3 and 16], reviews RCIP in a standard setting. The Nyström discretization is assumed to rely on composite Gauss–Legendre quadrature with 16 nodes per quadrature panel.

We start with a Fredholm second kind BIE on  $\Gamma$  in standard form

$$(I + G) \rho(r) = g(r), \quad r \in \Gamma. \quad (20)$$

Here,  $G$  is an integral operator that is often assumed compact away from singular boundary points on  $\Gamma$ ,  $g(r)$  is a piecewise smooth right-hand side, and  $\rho(r)$  is the unknown layer density to be solved for.

For simplicity, we only discuss how to deal with one singular point on  $\Gamma$  and denote this point  $\gamma$ . Multiple singular points can be treated independently and in parallel.

Let  $G$  be split into two parts

$$G = G^\star + G^\circ, \quad (21)$$

where  $G^\star$  describes the kernel interaction close to  $\gamma$  and  $G^\circ$  is the (compact) remainder. Let the part of  $\Gamma$  on which  $G^\star$  is nonzero be denoted  $\Gamma^\star$ .

Now introduce the *transformed density*

$$\tilde{\rho}(r) = (I + G^\star) \rho(r). \quad (22)$$

Then use (21) and (22) to rewrite (20) as

$$(I + G^\circ(I + G^\star)^{-1}) \tilde{\rho}(r) = g(r), \quad r \in \Gamma. \quad (23)$$

Although (23) looks similar to (20), there are advantages to using (23) rather than (20) from a numerical point of view. For example, the spectral properties of  $G^\circ(I + G^\star)^{-1}$  are better than those of  $G$ .

The Nyström/RCIP scheme discretizes (23) chiefly on a grid on a *coarse mesh* on  $\Gamma$  that is sufficient to resolve  $G^\circ$ ,  $\tilde{\rho}(r)$ , and  $g(r)$ . Only the inverse  $(I + G^\star)^{-1}$  needs a grid on a locally refined *fine mesh* on  $\Gamma^\star$ . The fine mesh is obtained from the coarse mesh by  $n_{\text{sub}}$  times subdividing the coarse mesh in direction toward  $\gamma$ . The discretization of (23) assumes the form

$$(\mathbf{I}_{\text{coa}} + \mathbf{G}_{\text{coa}}^\circ \mathbf{R}) \tilde{\boldsymbol{\rho}}_{\text{coa}} = \mathbf{g}_{\text{coa}}, \quad (24)$$

where  $\mathbf{R}$  is a sparse block matrix called the *compressed inverse* and where the discrete unknown  $\tilde{\boldsymbol{\rho}}_{\text{coa}}$  lives on the coarse grid only. The boundary part  $\Gamma^\star$  is assumed to contain the two, four, or six coarse panels closest to  $\gamma$  depending on if  $\gamma$  is an endpoint, a corner, or a branch point.

The power of RCIP lies in the construction of  $\mathbf{R}$ . In theory,  $\mathbf{R}$  corresponds to a discretization of  $(I + G^\star)^{-1}$  on the fine grid, followed by a lossless compression back to the coarse grid. In practice,  $\mathbf{R}$  is constructed via a forward recursion of length  $n_{\text{sub}}$  on a hierarchy of intermediate grids on  $\Gamma^\star$ , and where refinement and compression occur in tandem. The computational cost grows, at most, linearly with  $n_{\text{sub}}$ .

Once the compressed equation (24) is solved for  $\tilde{\boldsymbol{\rho}}_{\text{coa}}$  and its *weight-corrected* counterpart

$$\hat{\boldsymbol{\rho}}_{\text{coa}} \equiv \mathbf{R} \tilde{\boldsymbol{\rho}}_{\text{coa}} \quad (25)$$

is produced, several useful functionals of  $\rho(r)$  can be computed with ease. Should one so wish, the solution  $\rho(r)$  on the fine grid can be reconstructed from  $\tilde{\boldsymbol{\rho}}_{\text{coa}}$  via a backward recursion on the same hierarchy of grids that is used in the construction of  $\mathbf{R}$ .

**Remark 1.** Note that the number of steps in the recursion for  $\mathbf{R}$  is the same as the number of subdivisions needed to create the fine mesh from the coarse

mesh and that this number is denoted  $n_{\text{sub}}$ . In the numerical experiments of Section 4 we shall illustrate the convergence of a field quantity as a function of  $n_{\text{sub}}$ .

**Remark 2.** The assumption, mentioned above, that  $G^\circ$  of (21) should be compact for RCIP to apply, is actually too restrictive. See [19, Eq. (24)] for a better, although more technical, assumption about  $G^\circ$ . Allowing  $G^\circ$  of (21) to be non-compact is important in the present work. In (31) we view  $B$  as a reasonable right preconditioner to  $A$  and merely consider  $(A(-B) - I)^\circ$  as an operator whose spectrum is clustered.

### 2.5. On-surface and near-field evaluation

The discretization of our BIEs on  $\Gamma$  involves the discretization of integrals with various types of singular integrands. Furthermore, for  $r$  close to  $\Gamma$ , the discretization of the field representations involves various types of nearly singular integrands. These singular and nearly singular integrals can, typically, not be accurately evaluated at a reasonable cost using composite standard interpolatory quadrature, but require special discretization techniques. For this, we use a panel-based product integration scheme which, according to the classification of [18], is “explicit split”.

Our panel-based explicit-split quadrature scheme is described in detail in [22, Section 4]. For now, we only mention that the scheme combines recursion with analytical methods such as the use of the fundamental theorem of complex line integrals. Nearly singular and singular integral operator kernels  $G(r, r')$  are split according to the general pattern

$$G(r, r') d\ell' = G_0(r, r') d\ell' + \log |r - r'| G_L(r, r') d\ell' + c_C \Re \left\{ \frac{G_C(z, t) dt}{i(t - z)} \right\} + \Re \left\{ \frac{G_H(z, t) dt}{i(t - z)^2} \right\}. \quad (26)$$

Here  $c_C$  is a, possibly complex, constant and  $G_0(r, r')$ ,  $G_L(r, r')$ ,  $G_C(z, t)$ , and  $G_H(z, t)$  are smooth functions. Our scheme requires explicit formulas for  $G(r, r')$ ,  $G_L(r, r')$ ,  $G_C(z, t)$ , and  $G_H(z, t)$ , while  $G_0(r, r')$  needs only to be known in the limit  $r' \rightarrow r$ . See [2, Section 6.2] for additional remarks.

## 3. The new numerical scheme

### 3.1. Integral representations and boundary integral equations

For the Dirichlet problem, we represent the field  $u(r)$  via

$$u(r) = S_k(-T_k)\rho(r), \quad r \in \mathbb{R}^2. \quad (27)$$

The BIE is

$$S_k(-T_k)\rho(r) = g(r), \quad r \in \Gamma. \quad (28)$$

For the Neumann problem, the field is represented via

$$u(r) = K_k(-S_k)\rho(r), \quad r \in \mathbb{R}^2 \setminus \Gamma, \quad (29)$$

and the BIE is

$$T_k(-S_k)\rho(r) = g(r), \quad r \in \Gamma. \quad (30)$$

We would like to comment on some differences between the BIEs (28,30) and (17,19) in [6]. First, the hypersingular integral operator  $T_k$  is used as the right preconditioner in our representation. The modification is somewhat trivial, but it removes the need to evaluating the action of  $T_k$  on the boundary data  $g$  in [6]. This is important when the open curves contain corners and branch points, as otherwise one would need to apply proper weight functions in  $T_k$  to ensure that the modified right-hand side is piecewise smooth. Second, the weight function  $\omega$  is completely removed from the integral representations (27,29). At the first sight, this may seem like a setback, as the strong inverse square root singularity changes the underlying function space for the density, and the BIEs (28,30) are no longer of the second kind.

However, as observed in [17],  $S_k$  and  $T_k$  are good preconditioners for each other pointwise, except at singular points. Thus, the BIEs (28,30) will be well-conditioned if the density singularities in the vicinity of those singular points (that is, endpoints, corners, and branch points) can be treated effectively. This is where the RCIP method comes into play.

### 3.2. Incorporating the RCIP into the BIEs (28,30)

The BIEs (28) and (30) are cast in the form

$$A(-B)\rho_1(r) = g(r), \quad r \in \Gamma, \quad (31)$$

where the unknown density now is denoted  $\rho_1(r)$  and where the integral operators  $A$  and  $B$  are either  $S_k$  and  $T_k$  or  $T_k$  and  $S_k$ . Clearly, the composition of  $A$  and  $-B$  and the absence of the identity operator make (31) look quite different from the standard form (20).

We now apply the Nyström/RCIP scheme of Section 2.4 to (31), with the goal to find the analogue of the compressed discrete equation (24) for (31). First, introduce a temporary density  $\rho_2(r)$  via

$$\rho_2(r) = -B\rho_1(r). \quad (32)$$

This allows us to rewrite (31) as the  $2 \times 2$  block system

$$\left( \begin{bmatrix} I & 0 \\ 0 & I \end{bmatrix} + \begin{bmatrix} -I & A \\ B & 0 \end{bmatrix} \right) \begin{bmatrix} \rho_1(r) \\ \rho_2(r) \end{bmatrix} = \begin{bmatrix} g(r) \\ 0 \end{bmatrix}, \quad (33)$$

which corresponds to (20) in Section 2.4.

Note that (33) is free from composed operators so that the standard RCIP method can be readily applied. The analogue of (23) is

$$\left( \begin{bmatrix} I & 0 \\ 0 & I \end{bmatrix} + \begin{bmatrix} -I^\circ & A^\circ \\ B^\circ & 0 \end{bmatrix} \left( \begin{bmatrix} I & 0 \\ 0 & I \end{bmatrix} + \begin{bmatrix} -I^\star & A^\star \\ B^\star & 0 \end{bmatrix} \right)^{-1} \right) \begin{bmatrix} \tilde{\rho}_1(r) \\ \tilde{\rho}_2(r) \end{bmatrix} = \begin{bmatrix} g(r) \\ 0 \end{bmatrix}. \quad (34)$$

The analogue of (24) is

$$\left( \begin{bmatrix} \mathbf{I}_{\text{coa}} & \mathbf{0}_{\text{coa}} \\ \mathbf{0}_{\text{coa}} & \mathbf{I}_{\text{coa}} \end{bmatrix} + \begin{bmatrix} -\mathbf{I}_{\text{coa}}^\circ & \mathbf{A}_{\text{coa}}^\circ \\ \mathbf{B}_{\text{coa}}^\circ & \mathbf{0}_{\text{coa}} \end{bmatrix} \begin{bmatrix} \mathbf{R}_1 & \mathbf{R}_3 \\ \mathbf{R}_2 & \mathbf{R}_4 \end{bmatrix} \right) \begin{bmatrix} \tilde{\boldsymbol{\rho}}_{1\text{coa}} \\ \tilde{\boldsymbol{\rho}}_{2\text{coa}} \end{bmatrix} = \begin{bmatrix} \mathbf{g}_{\text{coa}} \\ \mathbf{0}_{\text{coa}} \end{bmatrix}. \quad (35)$$

Here we have partitioned the compressed inverse  $\mathbf{R}$  into the four sparse equi-sized blocks  $\mathbf{R}_1$ ,  $\mathbf{R}_2$ ,  $\mathbf{R}_3$ , and  $\mathbf{R}_4 = \mathbf{I}_{\text{coa}}^\circ$ .

As an extra twist, we write the compressed equation (35) as a linear system involving only one discrete density – not two. To this end, introduce the new density  $\tilde{\boldsymbol{\rho}}_{\text{coa}}$  via

$$\begin{aligned} \tilde{\boldsymbol{\rho}}_{1\text{coa}} &= \tilde{\boldsymbol{\rho}}_{\text{coa}} + \mathbf{R}_1^{-1} \mathbf{R}_3 \mathbf{B}_{\text{coa}}^\circ \mathbf{R}_1 \tilde{\boldsymbol{\rho}}_{\text{coa}}, \\ \tilde{\boldsymbol{\rho}}_{2\text{coa}} &= -\mathbf{B}_{\text{coa}}^\circ \mathbf{R}_1 \tilde{\boldsymbol{\rho}}_{\text{coa}}. \end{aligned} \quad (36)$$

The change of variables (36) is chosen so that the second block-row equation of (35) is automatically satisfied. The first block-row equation of (35) becomes

$$\begin{aligned} (\mathbf{I}_{\text{coa}}^\star - \mathbf{A}_{\text{coa}}^\circ (\mathbf{R}_4 - \mathbf{R}_2 \mathbf{R}_1^{-1} \mathbf{R}_3) \mathbf{B}_{\text{coa}}^\circ \mathbf{R}_1 + \mathbf{A}_{\text{coa}}^\circ \mathbf{R}_2 \\ + \mathbf{R}_1^{-1} \mathbf{R}_3 \mathbf{B}_{\text{coa}}^\circ \mathbf{R}_1) \tilde{\boldsymbol{\rho}}_{\text{coa}} = \mathbf{g}_{\text{coa}}. \end{aligned} \quad (37)$$

We observe, from (36), that away from  $\Gamma^\star$  the discrete density  $\tilde{\boldsymbol{\rho}}_{\text{coa}}$  coincides with  $\tilde{\boldsymbol{\rho}}_{1\text{coa}}$ . Therefore one can expect the system (37) to share more properties with the original equation (31) than the expanded system (35) does. Numerical experiments indicate that (37) is superior to (35) not only in terms of computational economy, but also in terms of stability and of convergence of iterative solvers.

The analogue of (25) is

$$\begin{aligned} \hat{\boldsymbol{\rho}}_{1\text{coa}} &= \mathbf{R}_1 \tilde{\boldsymbol{\rho}}_{\text{coa}}, \\ \hat{\boldsymbol{\rho}}_{2\text{coa}} &= \mathbf{R}_2 \tilde{\boldsymbol{\rho}}_{\text{coa}} - (\mathbf{R}_4 - \mathbf{R}_2 \mathbf{R}_1^{-1} \mathbf{R}_3) \mathbf{B}_{\text{coa}}^\circ \mathbf{R}_1 \tilde{\boldsymbol{\rho}}_{\text{coa}}. \end{aligned} \quad (38)$$

### 3.3. Some algorithmic details

As mentioned in Section 2.4, Nyström discretization is used for integral equations. It relies solely on composite 16-point Gauss–Legendre quadrature and product integration based on polynomial interpolation as described in Section 2.5. We use the low-threshold stagnation-avoiding GMRES of [24, Section 8] to solve the resulting linear system, with the matrix-vector product accelerated by the FMM. The FMM computes the sum of the following form

$$u_i = \sum_{j=1}^N K(r_i, r'_j) q_j, \quad j = 1, \dots, N, \quad i = 1, \dots, M, \quad (39)$$

where  $K$  is a kernel function,  $M$  is the number of target points, and  $N$  is the number of source points. For highly oscillatory Helmholtz kernels, the cost is  $O((M+N) \log(M+N))$  [10, 16]. When the set of target points is identical to

the set of source points, the self-interaction terms  $j = i$  are excluded as most kernels are singular at the origin.

We use the single-layer potential operator  $S_k$  as an illustration of computational complexity in the context of solving discretized integral equations. To avoid cumbersome indices, we denote the matrix discretization of the operator  $S_k^\circ$  simply as  $\mathbf{S}^\circ$ . In order to apply  $\mathbf{S}^\circ$  fast to a given vector, we split it into two parts:

$$\mathbf{S}^\circ = \mathbf{S}_{\text{smooth}}^\circ + \mathbf{S}_{\text{qc}}^\circ, \quad (40)$$

where  $\mathbf{S}_{\text{smooth}}^\circ$  is obtained by discretizing  $S_k^\circ$  via standard Gauss-Legendre quadrature on each panel, and  $\mathbf{S}_{\text{qc}}^\circ$  is the quadrature correction part due to the logarithmic singularity of the kernel. We further write  $\mathbf{S}_{\text{smooth}}^\circ$  as

$$\mathbf{S}_{\text{smooth}}^\circ = \mathbf{S}_{\text{smooth}} - \mathbf{S}_{\text{smooth}}^*. \quad (41)$$

Since the weights are functions of the source point  $r'$  only, it is clear that the action of  $\mathbf{S}_{\text{smooth}}$  can be taken by the FMM. The quadrature correction part  $\mathbf{S}_{\text{qc}}^\circ$  depends on both the target and source points, but it is nonzero only for target points close to the panel for each source panel. Furthermore, the bad part  $\mathbf{S}_{\text{smooth}}^*$  is nonzero for panels that are near the singular points. Thus, both  $\mathbf{S}_{\text{qc}}^\circ$  and  $\mathbf{S}_{\text{smooth}}^*$  are sparse and can be constructed and applied in  $O(N)$  time and storage for most geometries. Combining all this, we observe that  $\mathbf{S}^\circ$  can be applied in  $O(N \log N)$  time. The preconditioner  $\mathbf{R}$  is the same as the identity matrix, except for the panels close to the singular points. The cost of constructing the nontrivial blocks of  $\mathbf{R}$  for each singular point is  $n_{\text{edge}}^3 n_{\text{gl}}^3 n_{\text{sub}}$ , where  $n_{\text{edge}}$  is the number of edges connected to the singular point,  $n_{\text{gl}}$  is the number of Gauss-Legendre nodes on each panel, and  $n_{\text{sub}}$  is the level of dyadic refinements along each edge in the forward recursion. Note that  $\mathbf{R}$  can be reused for identical geometries, for example, corners with the same opening angle, which is not uncommon in applications.

The evaluation of the field follows a similar approach. We decompose the operator into a smooth component and a quadrature correction component. The smooth part is computed using the FMM with  $O((N + M) \log(N + M))$  cost, while the quadrature correction is computed directly. Since only  $O(1)$  nearby targets require quadrature correction for each source panel, the cost of applying the correction is  $O(N + M)$  for typical applications. It is important to note that a sorting algorithm is needed to identify the targets requiring quadrature correction for each source panel. This can be done efficiently using either an adaptive quadtree [50] or a  $k$ -d tree (see, for example, [45, 55]).

#### 4. Numerical examples

The numerical codes used are implemented in MATLAB, release 2022a, and executed on a laptop equipped with eight Intel i9-10885H CPU Cores. We use the wideband Helmholtz FMM from the `fmm2d` [13] library, compiled with OpenMP enabled; the parallel efficiency ranges from 50% to 70%.

In most examples, the total field is given by  $u^{\text{tot}}(r) = u^{\text{in}}(r) + u^{\text{sc}}(r)$ , where  $u^{\text{in}}$  represents an incident plane wave

$$u^{\text{in}}(r) = e^{ik(x \cos \theta + y \sin \theta)} \quad (42)$$

with the incident angle  $\theta$ , and  $u^{\text{sc}}$  denotes the scattered field. We assume that the total field satisfies a zero boundary condition, which leads to an appropriate boundary condition for the scattered field, solved numerically. We begin with a coarse mesh on  $\Gamma$ , which is sufficient to resolve  $G^\circ$ ,  $\tilde{\rho}(r)$ , and  $g(r)$  to the prescribed tolerance. For field and error images in Figures 4, 7, 10, and 12, GMRES tolerance is set to  $10^{-13}$ . When assessing the accuracy of computed fields we adopt a procedure where, for each numerical solution, we also compute an overresolved reference solution, using approximately 50% more points in the discretization of the setup under study. Both the fields and their errors are computed at  $3000 \times 3000$  points on a Cartesian grid in the computational domains shown. The absolute difference between these two solutions at a field point is referred to as the *estimated absolute pointwise error*.

#### 4.1. Validation of the correctness of formulation and implementation

As there are no simple analytic solutions to the Helmholtz Dirichlet and Neumann problems on open curves, we use a Fortran code that implements the  $u(r) = S_k S_{0,I}^{-1} \rho(r)$  formulation for the Dirichlet problem (a straightforward extension of the formulation in [32] and also used in [6] as a comparison) to cross validate the correctness of the numerical scheme and its implementation in this paper. Here,  $S_{0,I}^{-1}$  is the inverse of the Laplace single layer potential operator on the straight line segment, which can be computed analytically for Chebyshev polynomials.

In this first example,  $\Gamma$  is the straight line segment parameterized as

$$r(s) = (s, -0.2), \quad s \in [-1, 1]. \quad (43)$$

The wavenumber is  $k = 3$ , the boundary data is

$$g(r) = 4x^3 + 2x^2 - 3x - 1, \quad (44)$$

and we seek  $u(r)$  at a target point  $r_{\text{targ}} = (0.17, 0.62)$ . The reference value

$$u_{\text{ref}} = 0.02788626934981090 - 0.75932847390327920i$$

for  $u(r_{\text{targ}})$  is obtained using 24-digit variable-precision arithmetic and 24-point composite Gauss–Legendre quadrature in the discretization of the formulation (27,28). The value produced by the Fortran code mentioned above agrees with  $u_{\text{ref}}$  to about 14 digits, thereby validating the correctness of both the formulation (27,28) itself and of our Nyström/RCIP discretization thereof.

Like all RCIP-based numerical schemes, the convergence of field quantities as a function of  $n_{\text{sub}}$  is an important measure on the stability and accuracy of our numerical scheme. Figure 1 shows that the error decreases to about  $2 \times 10^{-15}$  as

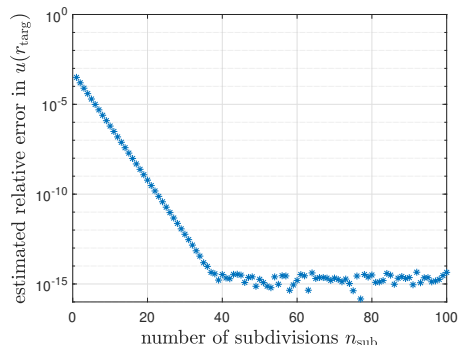


Figure 1: Convergence of  $u(r_{\text{targ}})$  with  $n_{\text{sub}}$  for the Helmholtz Dirichlet problem on the straight line segment (43).

$n_{\text{sub}}$  increases from 1 to 39, then fluctuates below  $10^{-14}$  afterwards all the way to  $n_{\text{sub}} = 100$ . Here the coarse mesh on  $\Gamma$  has 6 panels, that is, 96 discretization points. An estimated relative residual of machine epsilon ( $\epsilon_{\text{mach}}$ ) in double-precision floating point arithmetic is used as the GMRES stopping criterion (tolerance). The number of GMRES iterations needed for full convergence with the formulation (27,28) is 17. Since  $n_{\text{sub}}$  is the level of dyadic refinement towards the endpoints and  $\epsilon_{\text{mach}} = 2^{-52}$ , Figure 1 clearly shows that our numerical scheme is as stable and accurate as the standard RCIP method applied to an explicit SKIE, even though a hypersingular integral operator is used in the formulation. Furthermore, there is no GMRES stagnation, even though the formulation does not possess the so-called numerical second-kindness in [1].

#### 4.2. Comparison with the results in [6]

In this section, we present conditioning and timing results on a straight line segment and a spiral that are directly comparable with [6, Tables 2–5]. The total number of discretization points on  $\Gamma$  is  $N$ .

In [6] a global spectral method is used to discretize SKIEs (17,19), the whole system matrix is built using FFT in  $O(N^2 \log N)$  time, and the resulting linear system is then solved using GMRES. The prescribed precision is  $10^{-5}$ . However, it is not clear whether the field is also computed to precision  $10^{-5}$ , since there is no mentioning about the special quadrature on the close evaluation of the field and the number of points used in generating field plots [6, Figure 3]. The timing is measured via MATLAB’s command pair `tic` and `toc`.

In our numerical experiments, the GMRES tolerance is set to  $10^{-6}$ , the field is evaluated at  $300 \times 300$  equispaced tensor grid on a rectangle. We vary the wavenumber  $k$  so that the ratio  $L/\lambda = 50 \cdot 2^i$  for  $i = 0, 1, \dots, 9$ , where  $L$  is the arc length of  $\Gamma$  and  $\lambda = 2\pi/k$  is the wavelength. It is clear that the cases  $L/\lambda = 50, 200, 800$  presented in [6, Tables 2–5] is a subset of what we study here. We estimate the relative  $l_2$  error by comparing with a reference solution

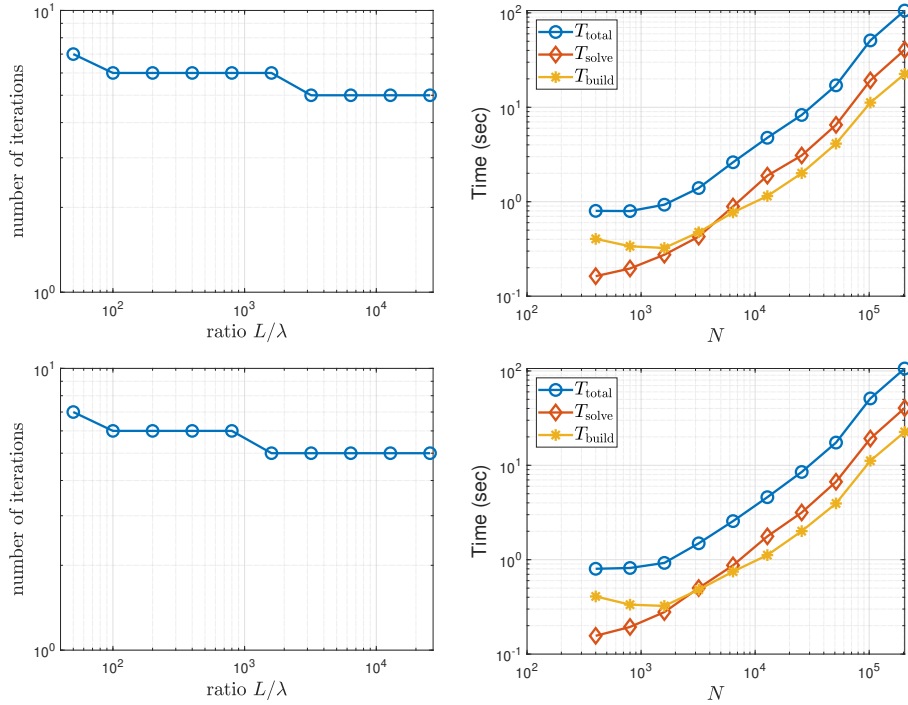


Figure 2: Number of GMRES iterations and computation times as a function of wavenumber for the Helmholtz problem on a straight line segment. Top: Dirichlet condition. Bottom: Neumann condition. Left: Number of GMRES iterations as a function of  $L/\lambda$ . Right: timing results as a function of  $N$  – the total number of discretization points on  $\Gamma$ . Here,  $\Gamma$  is divided into equi-sized panels in the parameter space and 16 Gauss-Legendre nodes are used to discretize each panel.  $N = 8L/\lambda$  for this example. The relative  $l_2$  error is measured on a  $300 \times 300$  tensor grid over the square  $[-1.3, 1.3] \times [-1.5, 1.1]$ . The largest relative  $l_2$  errors are about  $4 \times 10^{-7}$  for the Dirichlet problem and  $6 \times 10^{-7}$  for the Neumann problem.

obtained by increasing  $N$  and  $n_{\text{sub}}$  by about 50% each. That is,

$$E_2 = \frac{\|u_{\text{num}} - u_{\text{ref}}\|_2}{\|u_{\text{ref}}\|_2}. \quad (45)$$

#### 4.2.1. Straight line segment

Figure 2 shows the conditioning and timings of our solver for the Helmholtz Dirichlet and Neumann problems on the straight line segment (43), compare [6, Table 2] for the Dirichlet problem and [6, Table 4] for the Neumann problem. Here,  $T_{\text{total}}$  is the total computation time;  $T_{\text{build}}$  is the time on building the quadrature part of the system matrix  $\mathbf{S}_{\text{qc}}^{\circ}$  and  $\mathbf{T}_{\text{qc}}^{\circ}$ , the smooth part of the system matrix  $\mathbf{S}_{\text{smooth}}^*$  and  $\mathbf{T}_{\text{smooth}}^*$  in the vicinity of the singular points, and the preconditioner  $\mathbf{R}$ ; and  $T_{\text{solve}}$  is the time on GMRES. We observe that the Dirichlet problem is very similar to the Neumann problem in terms of both conditioning and timings. Amazingly, the number of points for achieving six

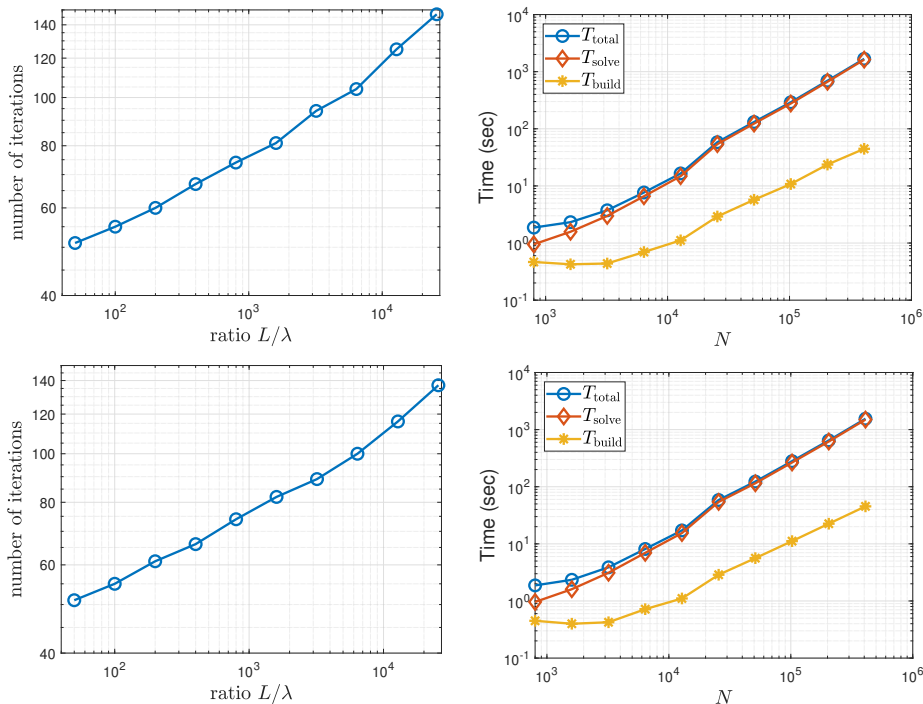


Figure 3: Same as Figure 2, but for the spiral defined by (46).  $N = 16L/\lambda$  for this example.

digits of accuracy for the straight line segment is exactly the same as that in [6] for achieving five digits of accuracy, even though we are using a panelwise discretization, while a global spectral method is used in [6]. In [6], the number of GMRES iterations is eight for the Dirichlet problem and nine for the Neumann problem, while one only needs at most seven iterations, and often only five or six, for both the Dirichlet and the Neumann problem with our scheme. This difference is certainly very minor, but it does demonstrate that our more general and purely numerical scheme performs as well as the analysis-based scheme in [6] in an example where the latter scheme is applicable.

For timings, both  $T_{\text{build}}$  and  $T_{\text{solve}}$  in our numerical methods are less than one second for  $L/\lambda = 800$ , while it takes more than 50 seconds for building the matrix and 14 seconds for solving the linear system in [6]. The difference will be larger for smaller wavelengths, requiring larger  $N$ , since our scheme scales like  $O(N)$  for  $T_{\text{build}}$ , and  $O(N_{\text{iter}}N \log N)$  for  $T_{\text{solve}}$ , with  $N_{\text{iter}}$  the number of iterations in GMRES, while the scheme in [6] scales like  $O(N^2 \log N)$  for  $T_{\text{build}}$  and  $O(N_{\text{iter}}N^2)$  for  $T_{\text{solve}}$ . We set  $n_{\text{sub}} = 40$  for computing the numerical solution and  $n_{\text{sub}} = 60$  for computing the reference solution. The time in computing  $\mathbf{R}$  is about 0.2 seconds for two endpoints.

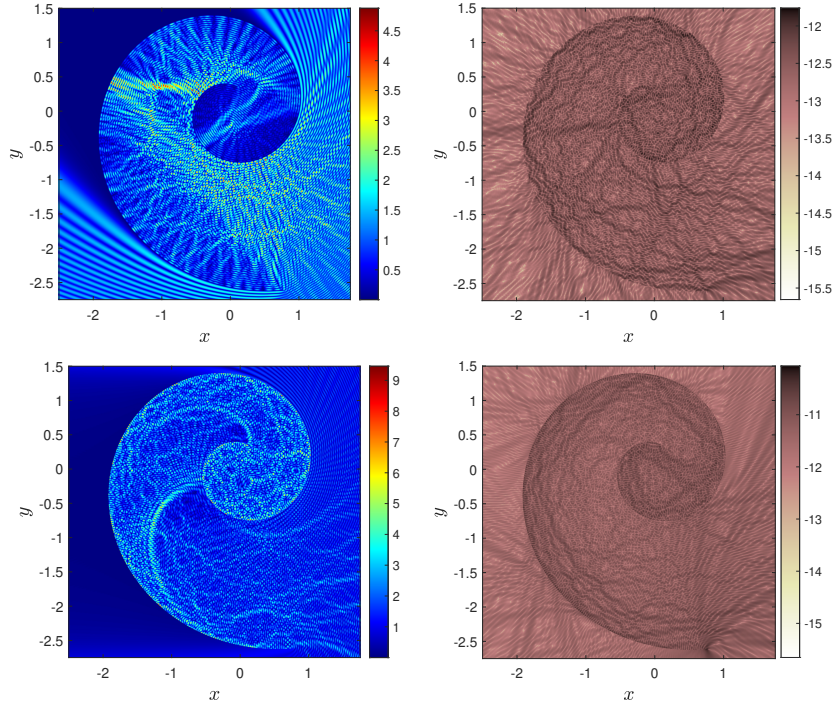


Figure 4: The magnitude of the total field  $|u^{\text{tot}}|$  and the estimate absolute error for the spiral with  $L/\lambda = 200$ , computed on a  $3000 \times 3000$  tensor grid over the rectangle  $[-2.5, 1.75] \times [-2.75, 1.5]$ . Top: Dirichlet condition. Bottom: Neumann condition. Left:  $|u^{\text{tot}}(r)|$ . Right:  $\log_{10}$  of the estimated absolute pointwise error in  $u^{\text{tot}}(r)$ .

#### 4.2.2. Spiral

Next,  $\Gamma$  is the logarithmic spiral in [6]

$$r(s) = (e^s \cos(5s), e^s \sin(5s)), \quad s \in [-1, 1]. \quad (46)$$

Figure 3 shows the conditioning and timings of our solver for the Helmholtz Dirichlet and Neumann problems on the spiral for  $L/\lambda$  up to 25600, compare [6, Table 3] for the Dirichlet problem and [6, Table 5] for the Neumann problem. The relative  $l_2$  error is measured on the square  $[-2.5, 1.75] \times [-2.75, 1.5]$ . The largest relative  $l_2$  errors are about  $3 \times 10^{-6}$  for the Dirichlet problem and  $2.7 \times 10^{-6}$  for the Neumann problem. The total number of discretization points is roughly twice of that used in [6]. Similar to [6], the number of iterations now increases as the wavenumber increases. For  $L/\lambda = 50, 200, 800$ ,  $N_{\text{iter}} = 51, 60, 74$  for the Dirichlet problem (compare  $N_{\text{iter}} = 46, 62, 79$  in [6, Table 3]), and  $51, 61, 74$  for the Neumann problem (compare  $48, 63, 83$  in [6, Table 5]). Furthermore, we observe that  $T_{\text{solve}}$  is very close to  $T_{\text{total}}$ , that is, the total computation time is dominated by the GMRES solve time. For  $L/\lambda = 800$ ,  $T_{\text{total}} \approx 17$  seconds for both the Dirichlet and Neumann problems with our scheme, while it takes about 160 seconds in [6].

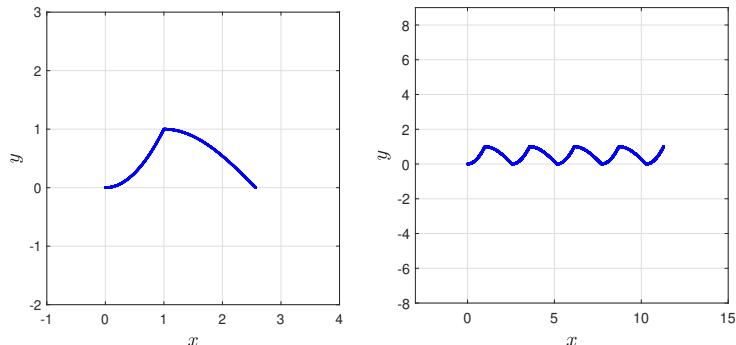


Figure 5: Boundary with corners. Left: one-corner curve defined by (47). Right: eight-corner curve by tiling the curve on the left four times horizontally.

Finally, Figure 4 presents high-resolution field images for the Dirichlet and Neumann problems with  $L/\lambda = 200$ . The incident field  $u^{\text{in}}$  is defined by (42), using an incident angle  $\theta = 3\pi/4$  for the Dirichlet problem and  $\theta = \pi$  for the Neumann problem. The boundary is divided into 440 equi-sized panels using arc-length parameterization, resulting in 7040 discretization points. GMRES converges to the prescribed tolerance of  $10^{-13}$  in 81 iterations for the Dirichlet problem and 79 iterations for the Neumann problem. The maximum absolute field error on a  $3000 \times 3000$  grid is estimated to be less than  $10^{-11}$ . Note that the image for the Dirichlet problem is directly comparable with the top image in [6, Figure 2].

### 4.3. Corners

We now consider boundaries with corners. The first boundary consists of a parabola and a cosine curve

$$r(s) = \begin{cases} (s, s^2), & s \in [0, 1], \\ (\frac{\pi s}{2}, \cos(\frac{\pi s}{2})), & s \in [0, 1], \end{cases} \quad (47)$$

which meet at the point  $(1, 1)$ . We also study boundaries with multiple corners. The left image of Figure 5 shows the one-corner curve (47). The right image shows an eight-corner curve obtained by horizontally tiling this curve four times.

Figure 6 presents the conditioning and timings of our solver for the Helmholtz Dirichlet and Neumann problems on the one-corner boundary, with  $L/\lambda$  up to 2560. The GMRES tolerance is set to  $10^{-12}$ . The relative  $l_2$  error is measured on a  $300 \times 300$  tensor grid over the square  $[-1.5, 4] \times [-2, 3.5]$ . The largest relative  $l_2$  errors are about  $6.4 \times 10^{-13}$  for the Dirichlet problem and  $1.2 \times 10^{-10}$  for the Neumann problem. We observe that the number of GMRES iterations increases mildly as the wavenumber increases, and that the timing is again dominated by  $T_{\text{solve}}$ . This indicates that our numerical scheme handles corners as effectively as endpoints.

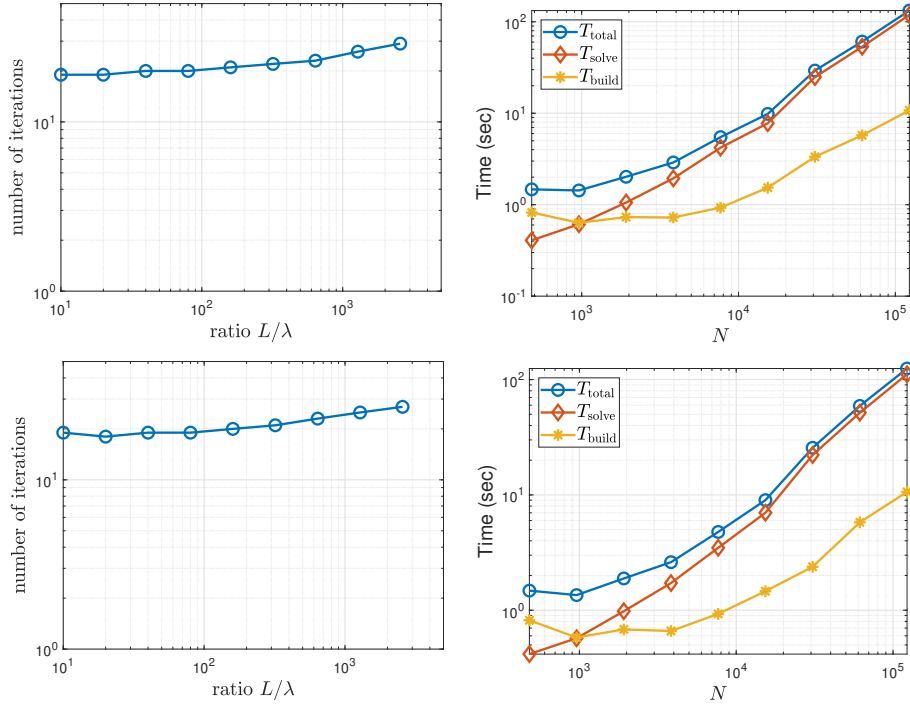


Figure 6: Same as Figure 2, but for the one-corner curve defined by (47).

Figure 7 presents high-resolution field images for the Dirichlet and Neumann problems on the eight-corner curve depicted in the right image of Figure 5, with  $L/\lambda = 200$  (corresponding to a wavenumber  $k = 83.58017152213590$ ). The images are computed on the rectangle  $[-3, 15] \times [-8, 9]$ . The incident field  $u^{\text{in}}$  is defined by (42), using an incident angle  $\theta = \pi/4$  for the Dirichlet problem and  $\theta = -\pi/4$  for the Neumann problem. The boundary is discretized into 9584 points, and the GMRES algorithm converges in approximately 40 iterations for both problems.

#### 4.4. Branch points

We now consider boundaries with branch points. The left image of Figure 8 shows a Y-shaped structure composed of three line segments with lengths 10, 8, and 8, and a top opening angle of  $\pi/2$ . The “tree” depicted in the right image is constructed recursively by reducing the branch lengths by a factor of 0.8 and decreasing the opening angles by dividing by 1.1 at each subsequent level.

Figure 9 illustrates the conditioning and computation times of our solver applied to the Helmholtz Dirichlet and Neumann problems on the Y shape depicted in the left image of Figure 8. The relative length  $L/\lambda$  ranges from 10 to 2560. The GMRES tolerance is set to  $10^{-12}$ . The relative  $l_2$  error is measured on a  $300 \times 300$  tensor grid over the square  $[-12, 12] \times [-3, 21]$ . The largest relative

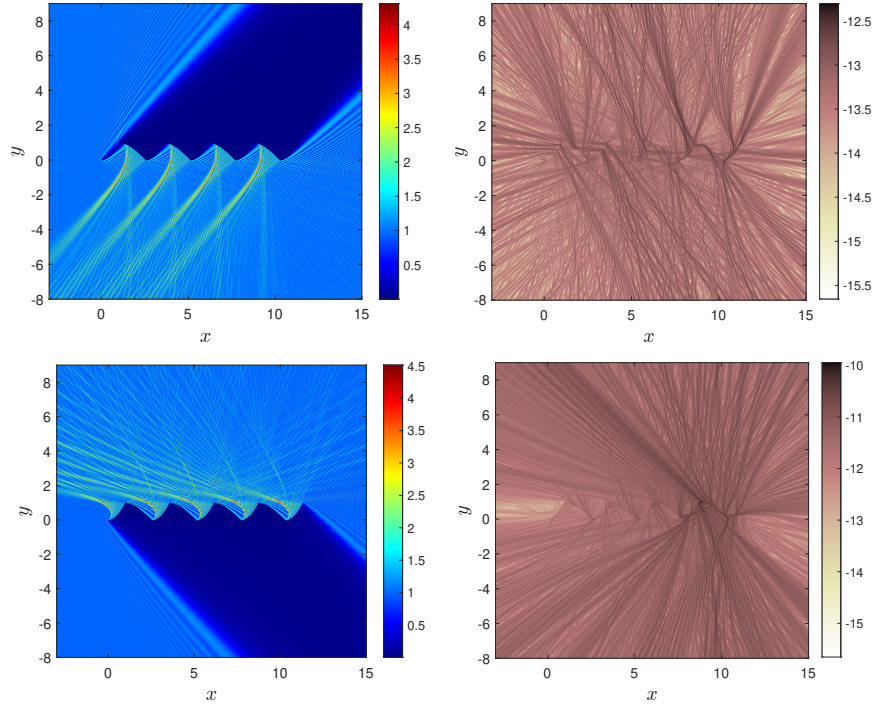


Figure 7: Same as Figure 4, but for the eight-corner curve.

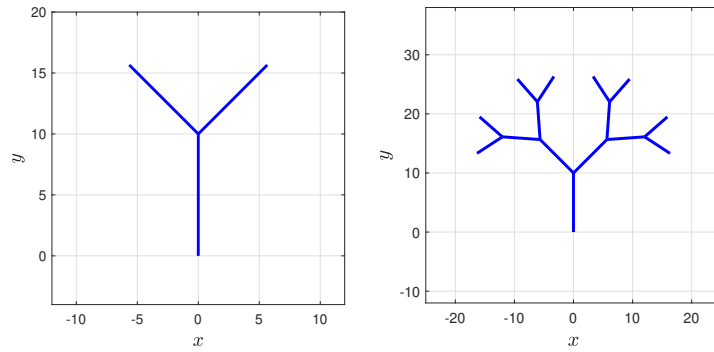


Figure 8: Branched boundary. Left: a Y shape. Right: a seven-branch curve with nine endpoints.

$l_2$  errors are about  $6.8 \times 10^{-13}$  for the Dirichlet problem and  $6.4 \times 10^{-11}$  for the Neumann problem. Similar to the line segment case, we observe that the number of GMRES iterations remains very stable as the wavenumber increases. Again, the computation time is dominated by  $T_{\text{solve}}$ , demonstrating that our numerical scheme handles branching structures as effectively as endpoints.

Figure 10 presents high-resolution field images for the Dirichlet and Neumann problems on the seven-branch curve depicted in the right image of Fig-

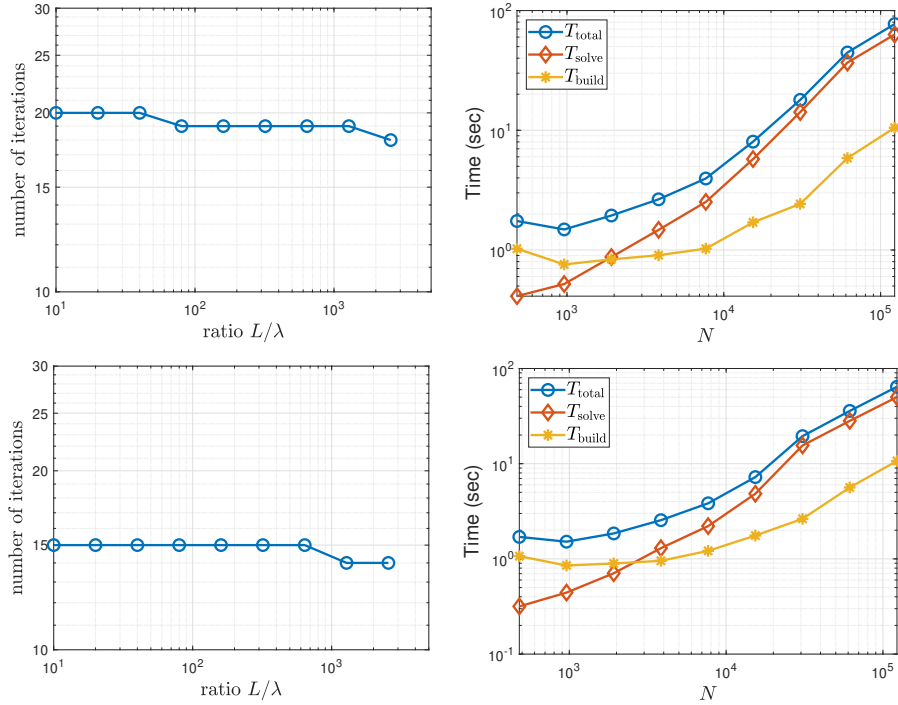


Figure 9: Same as Figure 2, but for the Y shape.

ure 8, with  $L/\lambda = 200$  (corresponding to a wavenumber  $k = 13.57645917713826$ ). The images are computed on the square  $[-25, 25] \times [-12, 38]$ . The incident field  $u^{\text{in}}$  is defined by (42), using an incident angle  $\theta = -2\pi/3$  for the Dirichlet problem and  $\theta = \pi/3$  for the Neumann problem. The boundary is discretized into 9552 points, and GMRES converges in 195 iterations for the Dirichlet problem and 193 iterations for the Neumann problem.

#### 4.5. A maze

Here, the boundary is a  $10 \times 10$  maze shown in Figure 11. It contains 30 endpoints, 31 corners, 18 triple junctions, and 2 quadruple junctions.

Figure 12 presents high-resolution field images for the Dirichlet problem on the maze with  $k = 10\pi$ . The incident field  $u^{\text{in}}$  is defined by (42), using an incident angle  $\theta = \pi/6$  for the Dirichlet problem and  $\theta = -2\pi/3$  for the Neumann problem. The images are computed on the square  $[-1, 11] \times [-1, 11]$ . The boundary is discretized into 28080 points. GMRES converges in 1877 iterations for the Dirichlet problem and 1815 iterations for the Neumann problem.

## 5. Conclusions and further discussions

We have constructed an integral-equation based numerical scheme for planar Helmholtz Dirichlet and Neumann problems on piecewise smooth open

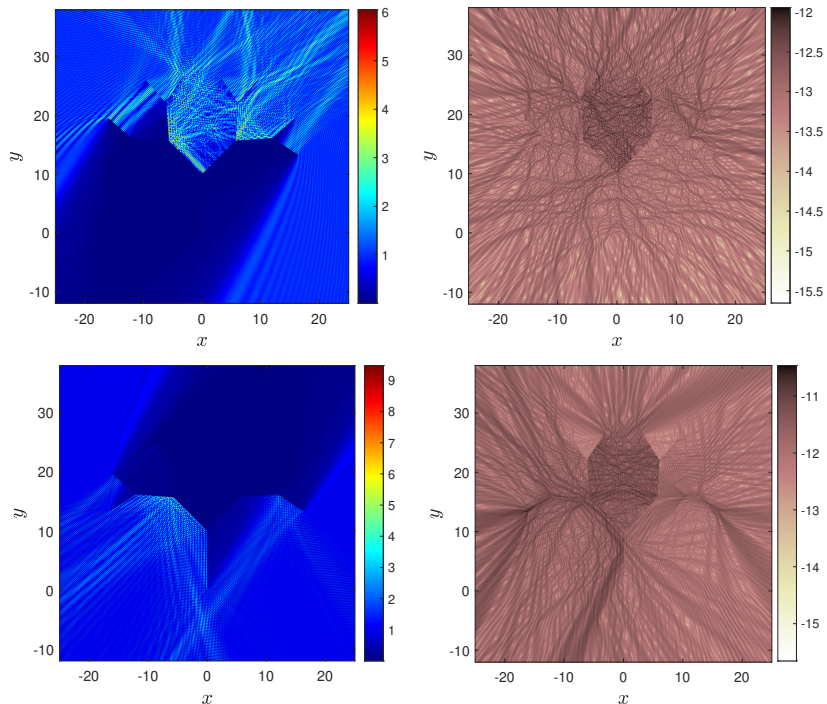


Figure 10: Same as Figure 4, but for the seven-branch curve.

curves. The accuracy produced by the scheme for medium-sized and medium-wavenumber problems is, roughly speaking, 11 digits with Dirichlet conditions and 10 digits with Neumann conditions. The RCIP method is a critical component of the scheme for handling the singularity of the unknown density in the BIE in the vicinity of singular points of arbitrary type, including endpoints, corners, and branch points. Since it is used to identify the correct function spaces of the unknown density, leading to stability and well-conditioning comparable to that obtained in [6] for smooth open curves, RCIP can, in a sense, be seen as a part of our integral equation formulation itself.

With the incorporation of the wideband fast multipole method, the computational cost is  $O(N \log N)$  for the matrix-vector product in each GMRES iteration and  $O((N + M) \log(N + M))$  for the evaluation of the field, where  $N$  is the number of source points on the boundary and  $M$  is the number of target points in the computational domain. As to the number of GMRES iterations, it depends on the geometry and wavenumber in a highly nontrivial way (see, for example, [37]). However, it is straightforward to replace the FMM with fast direct solvers [15, 27, 38, 39, 51, 54] to deal with frequency-scan problems, scattering with multiple right hand sides, and problems requiring large number of GMRES iterations. Some of these solvers can be investigated using excellent software packages such as FLAM [26] and `chunkie` [3]. Furthermore, we

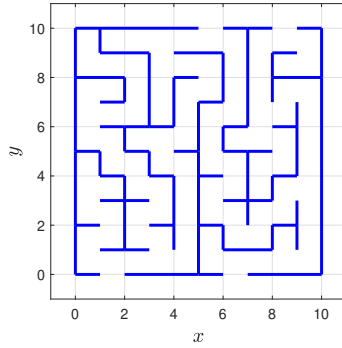


Figure 11: A maze-like boundary.

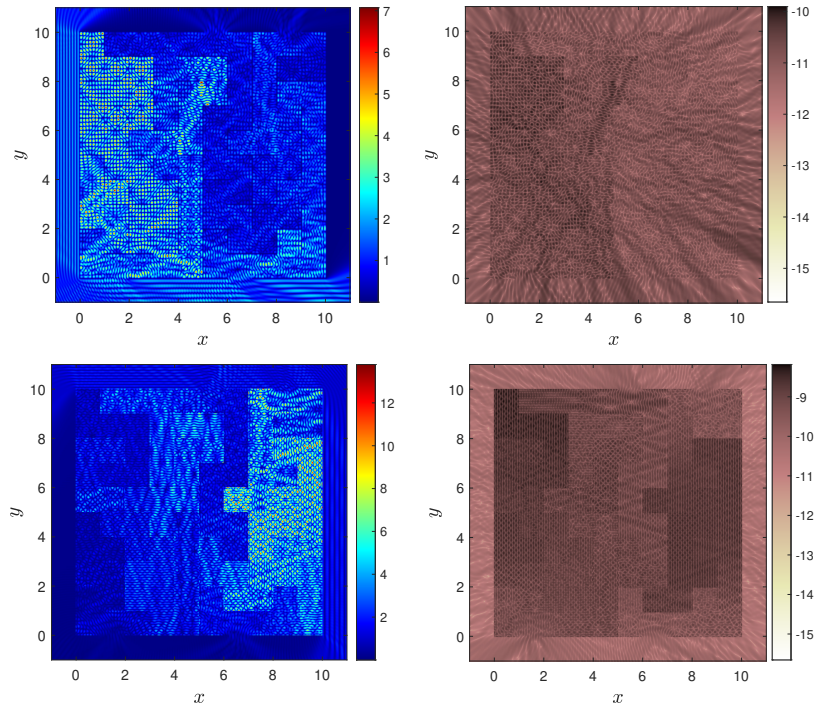


Figure 12: Same as Figure 4, but for the maze.

observe mild loss of accuracy in our scheme for some problems involving difficult geometries. These issues are currently under investigation.

The work in [6] has been extended to elastic scattering in two dimensions [7] recently and to three-dimensional acoustic and electromagnetic scattering in a preliminary report [52]. It is evident that our scheme can be extended to treat elastic scattering by piecewise smooth open curves in two dimensions. However, developing high-order efficient numerical schemes for open surface

problems in three dimensions is rather challenging. The high-order quadrature developed in [56] can be used to discretize associated layer potentials in three dimensions. Nevertheless, extending the RCIP method to handle corner and edge singularities in three dimensions remains an open problem (see [21, 25] for treatments of axially symmetric surfaces and a cube).

### Acknowledgement

This work was supported by the Swedish Research Council under contract 2021-03720.

### References

- [1] D. Agarwal, M. O’Neil, and M. Rachh. FMM-accelerated solvers for the Laplace–Beltrami problem on complex surfaces in three dimensions. *J. Sci. Comput.*, 97(1):25, 2023.
- [2] E. Andersson. Implementation and study of boundary integral operators related to PDE:s in the plane. Master’s Theses in Mathematical Sciences 2023:E27, Centre for Mathematical Sciences, Lund University, 2023. <https://lup.lub.lu.se/student-papers/record/9133621>.
- [3] T. Askham et al. chunkie: A MATLAB integral equation toolbox. <https://github.com/fastalgorithms/chunkie>, 2024.
- [4] A. H. Barnett and T. Betcke. Stability and convergence of the method of fundamental solutions for Helmholtz problems on analytic domains. *Journal of Computational Physics*, 227(14):7003–7026, 2008.
- [5] J. Bremer, Z. Gimbutas, and V. Rokhlin. A nonlinear optimization procedure for generalized Gaussian quadratures. *SIAM J. Sci. Comput.*, 32(4):1761–1788, 2010.
- [6] O. P. Bruno and S. K. Lintner. Second-kind integral solvers for TE and TM problems of diffraction by open arcs. *Radio Sci.*, 47(6): Paper No. RS6006, 13 pp., 2012.
- [7] O. P. Bruno, L. Xu, and T. Yin. Weighted integral solvers for elastic scattering by open arcs in two dimensions. *International Journal for Numerical Methods in Engineering*, 122(11):2733–2750, 2021.
- [8] A.-P. Calderón. Boundary value problems for elliptic equations. In *Proceedings of the Soviet-American Conference on Partial Differential Equations at Novosibirsk*, Fizmatgiz, Moscow, pages 303–304, 1963.
- [9] H. Cheng, W. Y. Crutchfield, Z. Gimbutas, L. Greengard, J. F. Ethridge, J. Huang, V. Rokhlin, N. Yarvin, and J. Zhao. A wideband fast multipole method for the Helmholtz equation in three dimensions. *J. Comput. Phys.*, 216:300–325, 2006.

- [10] H. Cheng, W. Y. Crutchfield, Z. Gimbutas, L. Greengard, J. Huang, V. Rokhlin, N. Yarvin, and J. Zhao. Remarks on the implementation of the wideband FMM for the Helmholtz equation in two dimensions. *Contemp. Math.*, 408(01):99–110, 2006.
- [11] D. Colton and R. Kress. *Inverse acoustic and electromagnetic scattering theory*, volume 93 of *Applied Mathematical Sciences*. Springer-Verlag, Berlin, second edition, 1998.
- [12] M. Costabel, M. Dauge, and R. Duduchava. Asymptotics without logarithmic terms for crack problems. *Communications in Partial Differential Equations*, 28(5 & 6):869–926, 2003.
- [13] Z. Gimbutas, L. Greengard, M. O’Neil, M. Rachh, and V. Rokhlin. *fmm2d software library*. <https://github.com/flatironinstitute/fmm2d>. Accessed: October, 2024.
- [14] H. Ginn and L. N. Trefethen. Lightning Helmholtz solver. *arXiv e-prints*, arXiv:2310.01665, 2023.
- [15] A. Gopal and P.-G. Martinsson. An accelerated, high-order accurate direct solver for the Lippmann-Schwinger equation for acoustic scattering in the plane. *Adv. Comput. Math.*, 48, 2022.
- [16] L. Greengard, J. Huang, V. Rokhlin, and S. Wandzura. Accelerating fast multipole methods for the Helmholtz equation at low frequencies. *IEEE Comput. Sci. Eng.*, 5(3):32–38, 1998.
- [17] F. Hang and S. Jiang. Generalized Poincaré–Bertrand formula on a hypersurface. *Applied and Computational Harmonic Analysis*, 27(1):100–116, 2009.
- [18] S. Hao, A. H. Barnett, P. G. Martinsson, and P. Young. High-order accurate methods for Nyström discretization of integral equations on smooth curves in the plane. *Adv. Comput. Math.*, 40(1):245–272, 2014.
- [19] J. Helsing. Solving integral equations on piecewise smooth boundaries using the RCIP method: a tutorial. *arXiv e-prints*, arXiv:1207.6737v10 [physics.comp-ph], revised 2022.
- [20] J. Helsing, S. Jiang, and A. Karlsson. Design of invisible finite planar waveguides loaded with periodic arrays of PEC barriers. *IEEE Journal on Multiscale and Multiphysics Computational Techniques*, pages 1–9, 2024.
- [21] J. Helsing and A. Karlsson. Determination of normalized electric eigenfields in microwave cavities with sharp edges. *Journal of Computational Physics*, 304:465–486, 2016.
- [22] J. Helsing and A. Karlsson. On a Helmholtz transmission problem in planar domains with corners. *J. Comput. Phys.*, 371:315–332, 2018.

- [23] J. Helsing and R. Ojala. Corner singularities for elliptic problems: integral equations, graded meshes, quadrature, and compressed inverse preconditioning. *J. Comput. Phys.*, 227(20):8820–8840, 2008.
- [24] J. Helsing and R. Ojala. On the evaluation of layer potentials close to their sources. *J. Comput. Phys.*, 227:2899–2921, 2008.
- [25] J. Helsing and K.-M. Perfekt. On the polarizability and capacitance of the cube. *Applied and Computational Harmonic Analysis*, 34(3):445–468, 2013.
- [26] K. L. Ho. FLAM - Fast linear algebra in MATLAB. <https://github.com/klho/FLAM>, 2016.
- [27] K. L. Ho and L. Ying. Hierarchical interpolative factorization for elliptic operators: Integral equations. *Comm. Pure Appl. Math.*, 69(7):1314–1353, 2016.
- [28] J. Hoskins and M. Rachh. On the discretization of Laplace’s equation with Neumann boundary conditions on polygonal domains. *Journal of Computational Physics: X*, 8:100072, 2020.
- [29] J. Hoskins and M. Rachh. On the solution of Laplace’s equation in the vicinity of triple junctions. *Pure and Applied Analysis*, 2(2):447–476, 2020.
- [30] J. G. Hoskins, V. Rokhlin, and K. Serkh. On the numerical solution of elliptic partial differential equations on polygonal domains. *SIAM Journal on Scientific Computing*, 41(4):A2552–A2578, 2019.
- [31] G. C. Hsiao and W. L. Wendland. *Boundary integral equations*. Springer, 2008.
- [32] S. Jiang and V. Rokhlin. Second kind integral equations for the classical potential theory on open surfaces. II. *J. Comput. Phys.*, 195(1):1–16, 2004.
- [33] P. Kolm, S. Jiang, and V. Rokhlin. Quadruple and octuple layer potentials in two dimensions I: Analytical apparatus. *Applied and Computational Harmonic Analysis*, 14(1):47–74, 2003.
- [34] R. Kress. *Linear Integral Equations*, volume 82 of *Applied Mathematical Sciences*. Springer–Verlag, Berlin, third edition, 2014.
- [35] S. K. Lintner and O. P. Bruno. A generalized Calderón formula for open-arc diffraction problems: theoretical considerations. *Proceedings of the Royal Society of Edinburgh Section A: Mathematics*, 145(2):331–364, 2015.
- [36] J. Ma, V. Rokhlin, and S. Wandzura. Generalized Gaussian quadrature rules for systems of arbitrary functions. *SIAM J. Numer. Anal.*, 33(3):971–996, 1996.

- [37] P. Marchand, J. Galkowski, E. A. Spence, and A. Spence. Applying GMRES to the Helmholtz equation with strong trapping: how does the number of iterations depend on the frequency? *Advances in Computational Mathematics*, 48(4):37, 2022.
- [38] V. Minden, A. Damle, K. L. Ho, and L. Ying. A technique for updating hierarchical skeletonization-based factorizations of integral operators. *Multiscale Model. Simul.*, 14:42–64, 2016.
- [39] V. Minden, K. L. Ho, A. Damle, and L. Ying. A recursive skeletonization factorization based on strong admissibility. *Multiscale Model. Simul.*, 15(2):768–796, 2017.
- [40] F. W. J. Olver, D. W. Lozier, R. F. Boisvert, and C. W. Clark, editors. *NIST Handbook of Mathematical Functions*. Cambridge University Press, May 2010.
- [41] M. Rachh and K. Serkh. On the solution of the Stokes equation on regions with corners. *Communications on Pure and Applied Mathematics*, 73(11):2295–2369, 2020.
- [42] V. Rokhlin. Diagonal Forms of Translation Operators for the Helmholtz Equation in Three Dimensions. *Appl. Comput. Harm. Anal.*, 1:82–93, 1993.
- [43] V. Rokhlin. Sparse diagonal forms for translation operators for the Helmholtz equation in two dimensions. *Applied and Computational Harmonic Analysis*, 5(1):36–67, 1998.
- [44] Y. Saad and M. H. Schultz. GMRES: a generalized minimal residual algorithm for solving nonsymmetric linear systems. *SIAM J. Sci. Statist. Comput.*, 7(3):856–869, 1986.
- [45] R. Saye. High-order methods for computing distances to implicitly defined surfaces. *Communications in Applied Mathematics and Computational Science*, 9(1):107–141, 2014.
- [46] K. Serkh. On the solution of elliptic partial differential equations on regions with corners II: Detailed analysis. *Applied and Computational Harmonic Analysis*, 46(2):250–287, 2019.
- [47] K. Serkh and V. Rokhlin. On the solution of elliptic partial differential equations on regions with corners. *Journal of Computational Physics*, 305:150–171, 2016.
- [48] K. Serkh and V. Rokhlin. On the solution of the Helmholtz equation on regions with corners. *Proceedings of the National Academy of Sciences*, 113(33):9171–9176, 2016.
- [49] E. P. Stephan. Boundary integral equations for screen problems in  $\mathbb{R}^3$ . *Integral Equations and Operator Theory*, 10:236–257, 1987.

- [50] H. Sundar, R. S. Sampath, and G. Biros. Bottom-up construction and 2 : 1 balance refinement of linear octrees in parallel. *SIAM J. Sci. Comput.*, 30:2675–2708, 2008.
- [51] D. Sushnikova, L. Greengard, M. O’Neil, and M. Rachh. FMM-LU: A fast direct solver for multiscale boundary integral equations in three dimensions. *Multiscale Modeling & Simulation*, 21(4):1570–1601, 2023.
- [52] C. Turc, A. Anand, O. Bruno, and J. Chaubell. Efficient solution of three-dimensional problems of acoustic and electromagnetic scattering by open surfaces. In *Proceedings of WAVES*, 2011.
- [53] N. Yarvin and V. Rokhlin. Generalized Gaussian quadratures and singular value decompositions of integral operators. *SIAM J. Sci. Comput.*, 20(2):699–718, 1998.
- [54] X. Ye, J. Xia, and L. Ying. Analytical Low-Rank Compression via Proxy Point Selection. *SIAM J. Matrix Anal. Appl.*, 41(3):1059–1085, 2020.
- [55] C. D. Yu, J. Huang, W. Austin, B. Xiao, and G. Biros. Performance optimization for the k-nearest neighbors kernel on x86 architectures. In *Proceedings of the International Conference for High Performance Computing, Networking, Storage and Analysis*, pages 1–12, 2015.
- [56] H. Zhu and S. Veerapaneni. High-order close evaluation of Laplace layer potentials: A differential geometric approach. *SIAM Journal on Scientific Computing*, 44(3):A1381–A1404, 2022.